Deep-learning based hologram classification for molecular diagnostics

Sung-Jin Kim[1], Bing Zhao[1], Hyungsoon Im[2,3], Jouha Min[2,3], Nuri Choi[1], Cesar M. Castro[2], Ralph Weissleder[2,3,4], Hakho Lee[2,4], Kwonmoo Lee[1]

[1]Department of Biomedical Engineering, Worcester Polytechnic Institute, Worcester, Massachusetts

[2]Center for Systems Biology, Massachusetts General Hospital, Boston, Massachusetts

[3]Department of Radiology, Massachusetts General Hospital, Boston, Massachusetts

[4]Department of Systems Biology, Harvard Medical School, Boston, Massachusetts

Correspondence

Kwonmoo Lee (klee@wpi.edu), Hakho Lee (hlee@mgh.harvard.edu)

ABSTRACT

Lens-free digital in-line holography (LDIH) is a promising microscopic tool that can overcome the limitations (e.g., field of view) of traditional lens-based microcopy. Images produced by LDIH, however, require extensive computation time to reconstruct objet images from complex diffraction patterns, which limits LDIH utility for point-of-care applications, particularly in resource limited settings. Here, we describe a new deep-learning (DL) based approach to process LDIH images in the context of cellular analyses. Specifically, we captured hologram images of cells surface-labeled with molecular-specific microbeads, and trained neural networks to classify these holograms without reconstruction. Using raw holograms as input, the trained networks could group individual cells according to the number of beads attached. Particularly, VGG-19 pretrained networks showed robust performance even with noisy experimental data. Combined with the developed DL approach, LDIH could be realized as low-cost, portable tool for point-of-care diagnostics.

INTRODUCTION

Lens-free digital in-line holography (LDIH) is a powerful imaging platform, overcoming the limitations of traditional microscopy[1-6]. LDIH records diffraction patterns of samples, from which original object images can be computationally recovered. This strategy enables LDIH to image a large area (~mm^2) and yet achieve high spatial resolution (~µm). Furthermore, the simplistic optical design allows for compact setups, consisting of an imager and a coherent light source. LDIH has been tested for potential point-of-care (POC) diagnoses. Recently, we have further advanced LDIH for molecular diagnostics (D3, digital diffraction diagnostics)[3] wherein cancer cells were labeled with immuno-microbeads, and bead-bound cells were counted for protein profiling.

A major hurdle to translating LDIH into POC tests is the need for extensive computational power. In principle, diffraction patterns can be back-propagated to reconstruct human-friendly object images. The bottleneck lies in the recovery of phase information, lost during the imaging process. It has been shown that this information can be numerically recovered through iterative optimization[1, 7-9], but the process is costly in computation time and requires high-end resources (e.g., graphical processing unit). To that end, we explored an alternative approach in which diagnostic information could be extracted from the raw hologram images. In this microbead-based assay, albeit imperceptible to human eyes, we reasoned that cell-bead objects could generate distinct hologram patterns recognizable by machine vision classifiers. Developing such a capacity would eliminate the need for image reconstruction, further advancing LDIH utility for POC operations.

We report on a new deep-leaning (DL) approach to LDIH image analysis. DL is a revolutionary technique for image classification that can automatically recognize and extract salient features without relying on human intervention[10-14]. We adopted DL to directly classify diffraction patterns generated from cells and microbeads. Specifically, algorithms were developed to i) recognize the diffraction patterns of cells labeled with microbeads and ii) group the cells according to the number of attached beads. We found that a pretrained deep learning approach offered highly reliable performance in hologram classification. Finally, when applied to experimental D3 images, the DL algorithm achieved high accuracy (94%), allowing for reconstruction-free image classification.

RESULTS AND DISCUSSION

System and assay setup

Figure 1A shows the schematic of D3 system[3]. As a light source, we used a light-emitting diode (LED; λ = 420 nm). The light passes through a circular aperture (diameter, 100 µm), generating a coherent spherical wave on the sample plane. The incidence light and the scattered light from the sample then interfere each other, and the resulting diffraction pattern is recorded by a CMOS

imager. The system has a unit (×1) optical magnification, thereby having a field-of-view equal to the imager size.

To enable molecular-specific cell detection, we used antibody-coated microbeads (diameter, 6 μm) for cell labeling. The number of attached beads is proportional to the expression level of a target marker, allowing for quantitative molecular profiling[3]. Hologram patterns from unlabeled and bead-bound cells have subtle differences that are hard to detect with human eyes (**Fig. 1B**). Only after image reconstruction can beads and cells be differentiated and counted; cells have high amplitude and phase values, whereas microbeads have negligible phase.

Comparison between conventional and DL approaches

Conventional LDIH reconstruction (**Fig. 2A**) requires multiple repetitions of back-propagation, constraint application, and transformation[7]. This iterative algorithm is computationally intensive, either incurring long processing time, or requiring high-end resources (e.g., graphical processing unit server) for faster results. Furthermore, human intervention is occasionally needed to correct for stray reconstruction (e.g., debris, twin images).

In contrast, the DL-based approach is a reconstruction-free classification method (**Fig. 2B**). As an off-line task, we first trained a network using annotated holograms of bead-bound cells. Once the training is complete, the network was used for on-line classification tasks; holograms, without any image preprocessing, were entered as an input.

Specifically, we prepared holograms and corresponding reconstruction images of bead-bound cells. In each image pair, individual cells were annotated according to the number of beads attached: class 1 (0 or 1 bead), class 2 (2 beads), and class 3 (>2 beads). About 80% of of data samples were used to train the network for classification. Following training, the rest of data was used as a testing set, measuring the network performance. This process was repeated to find optimal hyper-parameters for the highest accuracy.

Network architecture

To develop the optimal classifier, we compared three different models. The first one (PCA-SVM; **Fig. 3A**) was a conventional machine learning model. We used principal component analysis (PCA)[15] to reduce the image dimension. Two principle components were obtained from each image, and used as an input to support vector machine (SVM)[16]. The second model (**Fig. 3B**) was a basic convolutional neural network (CNN) [17] consisting of two convolutional layers and one fully-connected layer (**Fig. 3B**). After two connective convolution processes with a 3×3 convolutional filter, a 2×2 max pooling was conducted with the dropout rate P_d = 0.5. Then a 128-node fully-connected layer was applied (P_d = 0.5), followed by a 3-node output layer that produced a classification output with softmax activation function. Convolution layers and the 128-node layer included ReLU (Rectified Linear Unit) activation function. The third model (VGG19-FC; **Fig. 3C**) combined a pre-trained network (VGG-19)[12] and a fully connected layer.

We used the original VGG-19, unmodified from Keras Python DL Package, to simply extract features. The output was then fed into a 64-node layer with P_d = 0.7 and ReLU activation function.

Testing with synthetic hologram images

We first tested the feasibility of the reconstruction-free classification, using numerically generated data sets. The data generator (**Fig. 4A**) took two images, one containing a cell and the other a microbead; each image had both magnitude and phase information (**Fig. 4B**) obtained from hologram reconstruction. These inputs were then combined; the number of beads and their relative position on the cell were changed, mimicking cell labeling with microbeads. Finally, the combined images were transformed into holograms to simulate D3 measurements (**Fig. 4C**).

We trained all three classifying networks using both object images and synthetic holograms. With these synthetic data, all models achieved high accuracy (**Fig. 5A**). The overfitting was also minimal (**Figs. 5B, C**). Notably, VGG-19, which was pre-trained only with public ImageNet datasets, was still capable of extracting key features from holograms, making the classification effective. Overall, the results confirmed that i) bead-bound cells can be classified directly from holograms; and ii) classification of holograms can be accurate as with object images.

Classification with experimental datasets

We next evaluated the networks using experimental images taken by D3. Samples were prepared by labeling cancer cells (SkBr3, breast carcinoma) with polystyrene beads (diameter, 6 µm) conjugated with EpCAM antibodies. Labeled cells, suspended in buffer, were loaded on a microscope slide, and their holograms were imaged (**Fig. 6A, left**). To prepare the training set for classification, we reconstructed object images from holograms (**Fig. 6A, right**), and manually annotated cells with the number of bound beads. We obtained two training sets, one for holograms (**Fig. 6B**) and the other for object images (**Fig. 6C**). Each set had 179 images. Compared to the synthetic dataset, these images included noisy objects such as unbound beads and other surrounding cells.

The D3-generated sets were then used to train the classifying networks. Each network was trained for holograms or object images. **Figure 7A** summarizes the results. The overall accuracy of PCA-SVM and CNN classifiers decreased significantly, presumably due to real-world variations in data sets. In contrast, VGG-19-FC maintained high accuracy (94.4% for both holograms and object images; **Figs. 7B, C**) and had lower categorical cross-entropy loss than CNN. We further inspected VGG-19 performance by generating tSNE plots of input images (i.e., training sets) and their VGG-19 outputs. In both training sets (holograms, object images), each class of bead-bound cells were more segregated in VGG-19 outputs (**Fig. 8**), which helped more efficient classification in the downstream. It is conceivable that VGG-19, pre-trained withe large number of random images, is robust against noise and artifacts. Taken together, these results

demonstrate the feasibility of hologram classification without reconstruction in the experimental images, simplifying the workflow and decreasing computational cost.

CONCLUSIONS

We have demonstrated that DL networks can effectively classify holograms without reconstructing their original images. Our approach could free LDIH from extensive on-line computation, significantly advancing the utility of LDIH for point-of-care applications. Particularly, a pretrained DL approach shows significantly robust accuracy and loss performance in terms of the cell classification where we combined VGG-19 networks and a fully connected layer for advanced feature extraction and fine-tuned classification, respectively.

Acknowledgements. We thank NVIDIA for providing us with TITAN X GPU cards (NVIDIA Hardware Grant Program, K.L.) and Microsoft for Azure cloud computing resources (Microsoft Azure Research Award, K.L.). This work is supported by the WPI Start-up Fund for new faculty. The authors were supported in part by the WPI Start-up Fund for new faculty (K.L); gift by Boston Scientific (K.L); NIH grants R21-CA205322 (H.L.), R01-HL113156 (H.L.), R01-CA204019 (R.W.), R01-EB010011 (R.W.), R01-EB00462605A1 (R.W.), K99-CA201248-02 (H. I.); Liz Tilberis Award - Ovarian Cancer Research Fund (C.M.C); the Lustgarten Foundation (R.W.); and MGH Scholar Fund (H.L.).

Author Contributions. S.K. initiated the project, designed and trained the neural networks, and wrote the final version of the manuscript and supplement; B.Z performed training of CNNs. H.I. and J.M set up the imaging system and generated the hologram data; C.M.C and R.W coordinated the experiments with cancer cells; N.C. prepared the training set; K.L. and H.L. coordinated the study and wrote the final version of the manuscript and supplement. All authors discussed the results of the study.

Author Information. The authors declare no competing financial interests. Correspondence and requests for materials should be addressed to K.L. (klee@wpi.edu) and H. L. (hlee@mgh.harvard.edu)

References

1. Garcia-Sucerquia, J.; Xu, W.; Jericho, S. K.; Klages, P.; Jericho, M. H.; Kreuzer, H. J., Digital in-line holographic microscopy. *Appl Opt* **2006,** *45* (5), 836-50.

2. Greenbaum, A.; Luo, W.; Su, T. W.; Gorocs, Z.; Xue, L.; Isikman, S. O.; Coskun, A. F.; Mudanyali, O.; Ozcan, A., Imaging without lenses: achievements and remaining challenges of wide-field on-chip microscopy. *Nat Methods* **2012,** *9* (9), 889-95.

3. Im, H.; Castro, C. M.; Shao, H.; Liong, M.; Song, J.; Pathania, D.; Fexon, L.; Min, C.; Avila-Wallace, M.; Zurkiya, O.; Rho, J.; Magaoay, B.; Tambouret, R. H.; Pivovarov, M.; Weissleder, R.; Lee, H., Digital diffraction analysis enables low-cost molecular diagnostics on a smartphone. *Proc Natl Acad Sci U S A* **2015,** *112* (18), 5613-8.

4. Xu, W.; Jericho, M. H.; Meinertzhagen, I. A.; Kreuzer, H. J., Digital in-line holography for biological applications. *Proc Natl Acad Sci U S A* **2001,** *98* (20), 11301-5.

5. Gurkan, U. A.; Moon, S.; Geckil, H.; Xu, F.; Wang, S.; Lu, T. J.; Demirci, U., Miniaturized lensless imaging systems for cell and microorganism visualization in point-of-care testing. *Biotechnol J* **2011,** *6* (2), 138-49.

6. Greenbaum, A.; Luo, W.; Khademhosseinieh, B.; Su, T.-W.; Coskun, A. F.; Ozcan, A., Increased space-bandwidth product in pixel super-resolved lensfree on-chip microscopy. *Sci. Rep.* **2013,** *3*, 1717.

7. Fienup, J., Phase retrieval algorithms: a comparison. *Appl Opt* **1982,** *21* (15), 2758-69.

8. Mudanyali, O.; Tseng, D.; Oh, C.; Isikman, S. O.; Sencan, I.; Bishara, W.; Oztoprak, C.; Seo, S.; Khademhosseini, B.; Ozcan, A., Compact, light-weight and cost-effective microscope based on lensless incoherent holography for telemedicine applications. *Lab Chip* **2010,** *10* (11), 1417-28.

9. Mudanyali, O.; Oztoprak, C.; Tseng, D.; Erlinger, A.; Ozcan, A., Detection of waterborne parasites using field-portable and cost-effective lensfree microscopy. *Lab Chip* **2010,** *10* (18), 2419-23.

10. Srivastava, N.; Hinton, G. E.; Krizhevsky, A.; Sutskever, I.; Salakhutdinov, R., Dropout: a simple way to prevent neural networks from overfitting. *Journal of machine learning research* **2014,** *15* (1), 1929-1958.

11. LeCun, Y.; Bengio, Y.; Hinton, G., Deep learning. *Nature* **2015,** *521* (7553), 436-44.

12. Simonyan, K.; Zisserman, A., Very deep convolutional networks for large-scale image recognition. *International Conference on Learning Representations* **2015**.

13. Nguyen, T.; Bui, V.; Lam, V.; Raub, C. B.; Chang, L.-C.; Nehmetallah, G., Automatic phase aberration compensation for digital holographic microscopy based on deep learning background detection. *Optics Express* **2017,** *25* (13), 15043-15057.

14. Rivenson, Y.; Zhang, Y.; Gunaydin, H.; Teng, D.; Ozcan, A., Phase recovery and holographic image reconstruction using deep learning in neural networks. *arXiv preprint arXiv:1705.04286* **2017**.

15. Pearson, K., LIII. On lines and planes of closest fit to systems of points in space. *Philosophical Magazine* **1901,** *2* (11), 559-572.

16. Cortes, C.; Vapnik, V., Support-vector networks. *Machine learning* **1995,** *20* (3), 273-297.

17. LeCun, Y.; Boser, B. E.; Denker, J. S.; Henderson, D.; Howard, R. E.; Hubbard, W. E.; Jackel, L. D. In *Handwritten digit recognition with a back-propagation network*, 1990; pp 396-404.

FIGURES

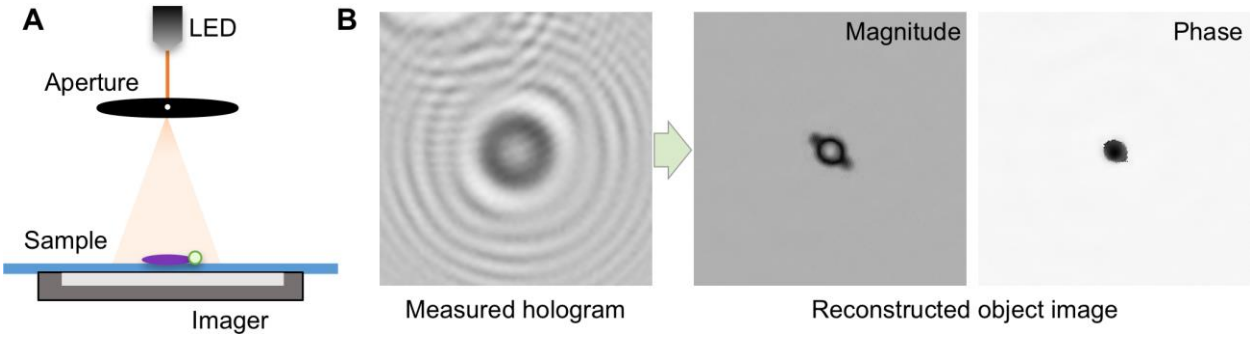

Figure 1. In-line holographic imaging. (A) A holography system includes LED, a sample glass and a sensor where a light is passed to a sample through a pinhole disk. **(B)** A hologram image and its associated reconstructed images consisting of magnitude and phase images.

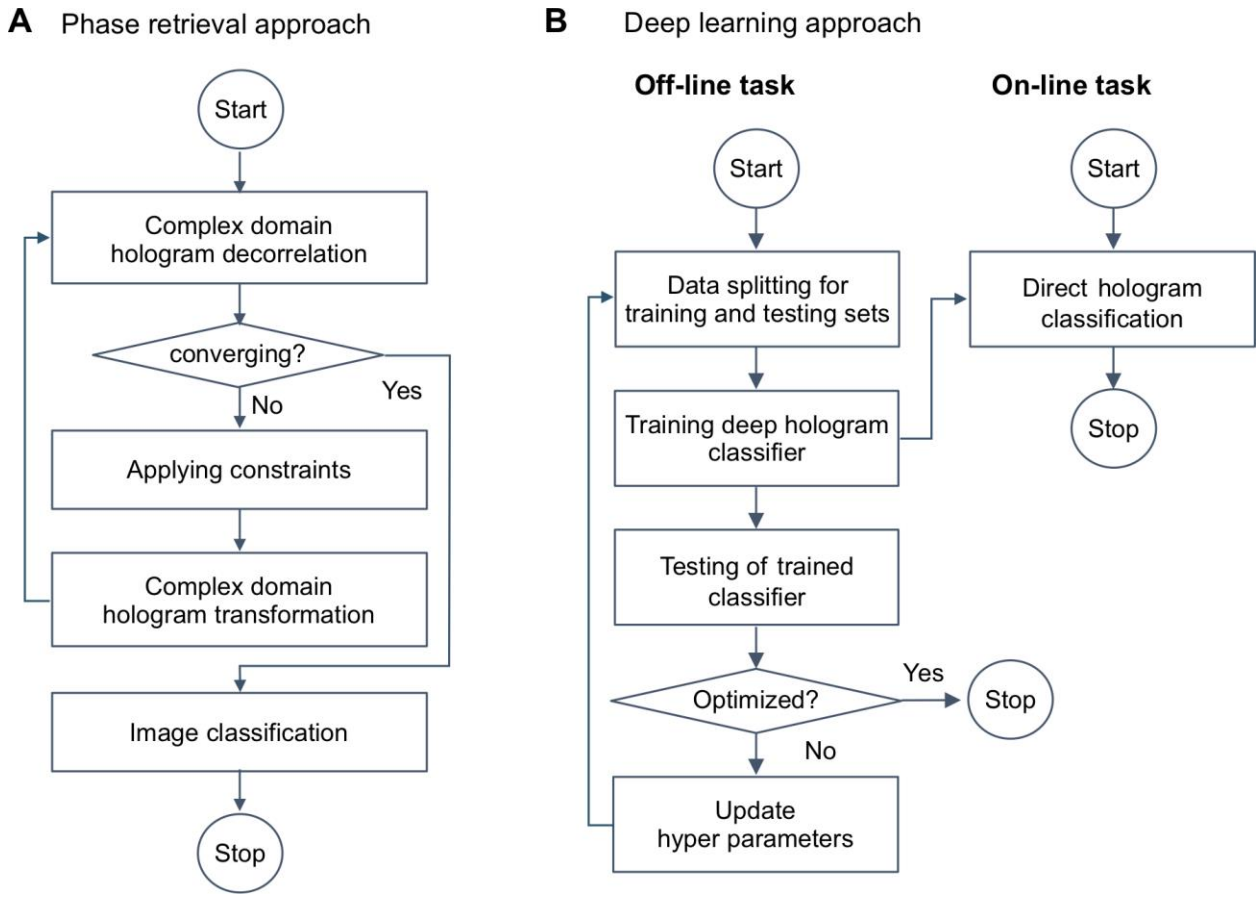

Figure 2. Flow charts of holographic classification approaches. **(A)** The conventional approach includes an iterative reconstruction process before image classification. **(B)** The machine learning based approach performs a training process before the classification stage.

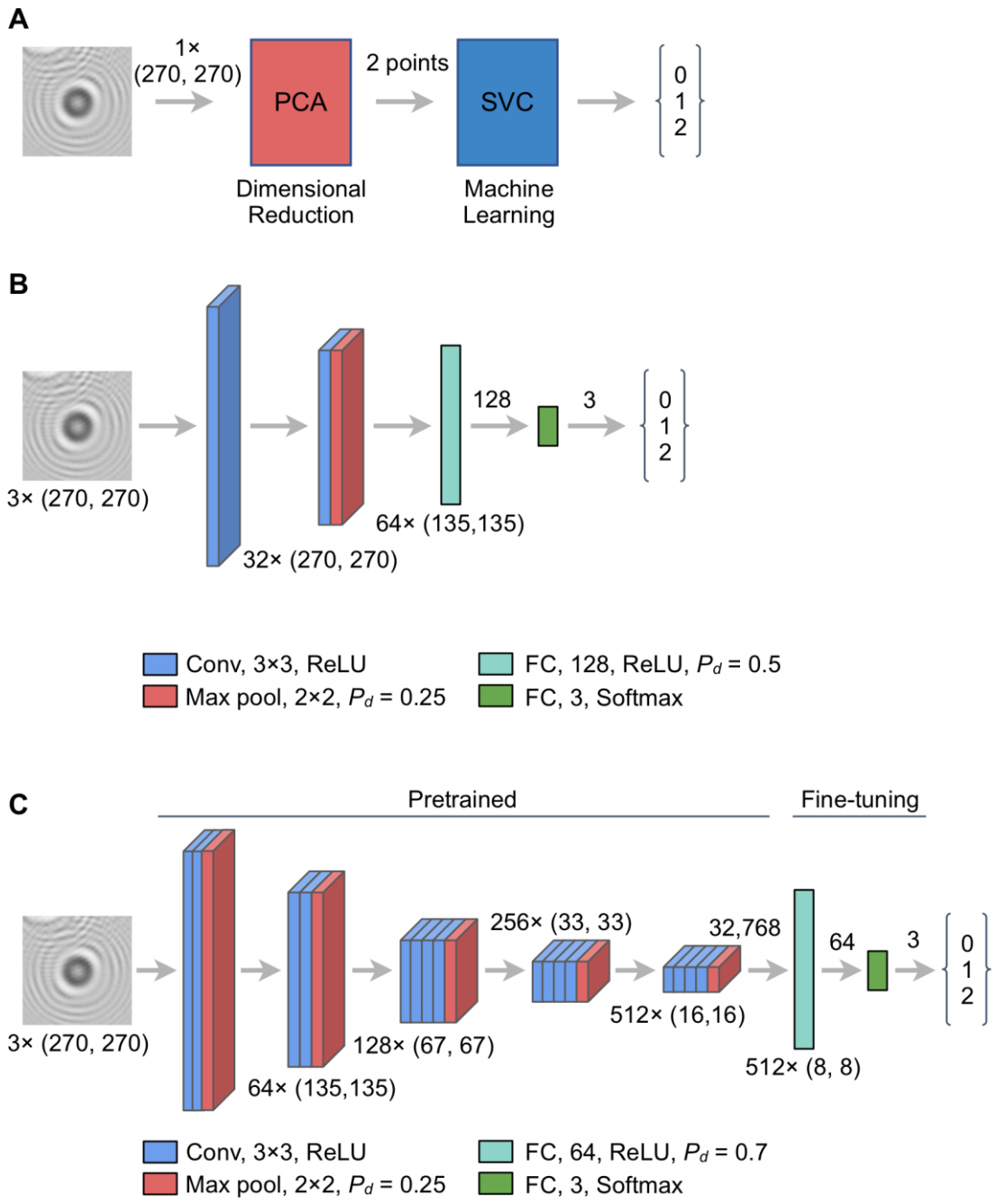

Figure 3. Machine learning approaches in this study. (A) The conventional machine learning approach consisting of PCA and SVM (PCA-SVM). **(B)** A basic convolutional network approach (CNN). **(C)** VGG-19 pretrained model-based approach (VGG-19-FC).

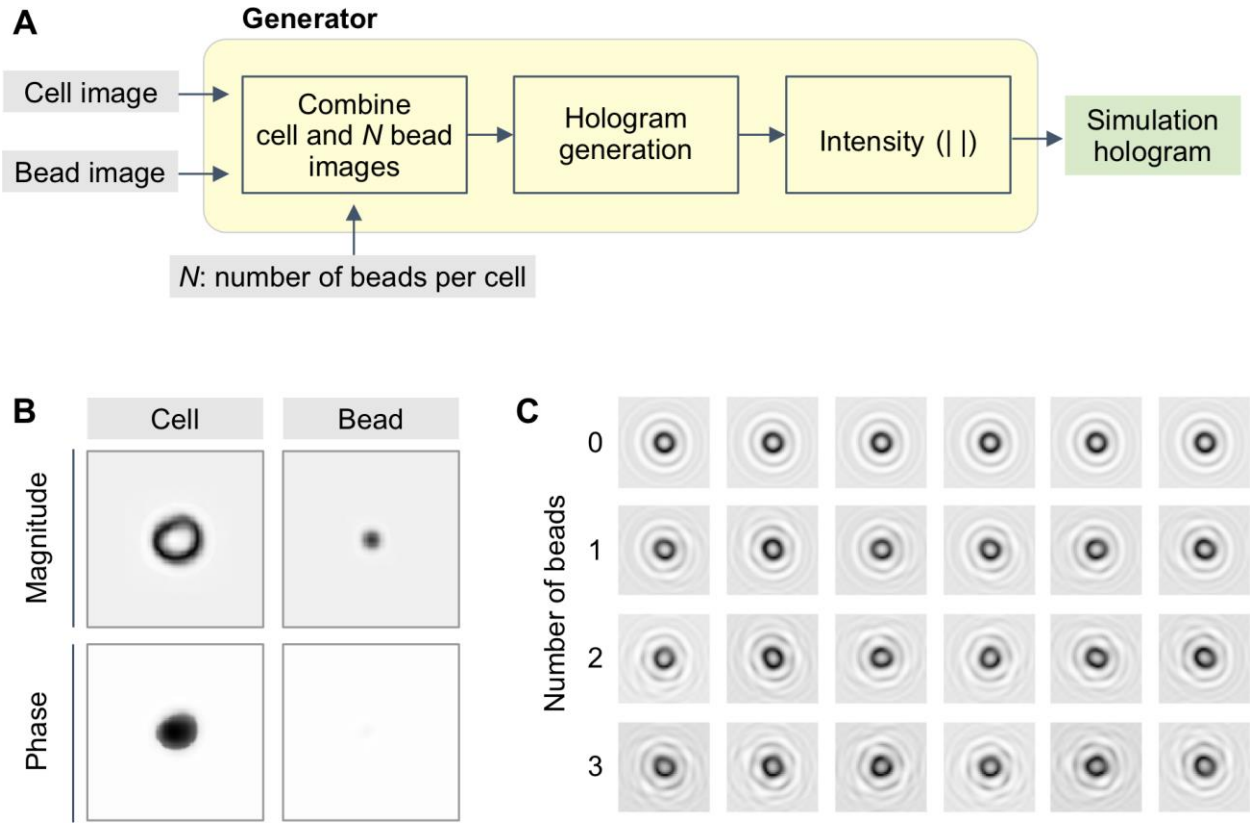

Figure 4. Synthesized holographic dataset. (A) Data synthesis workflow. **(B)** Experimental cell and bead images for synthesizing the data. **(C)** Synthesized hologram images.

A

	Accuracy (%)		Loss	
	Object image	Hologram	Object image	Hologram
SVM	57.3	58.5	-	-
PCA-SVM	98.4	99.8	-	-
CNN	100.0	100.0	0.0	0.0
VGG-19-FC	100.0	97.5	0.0	0.1

B

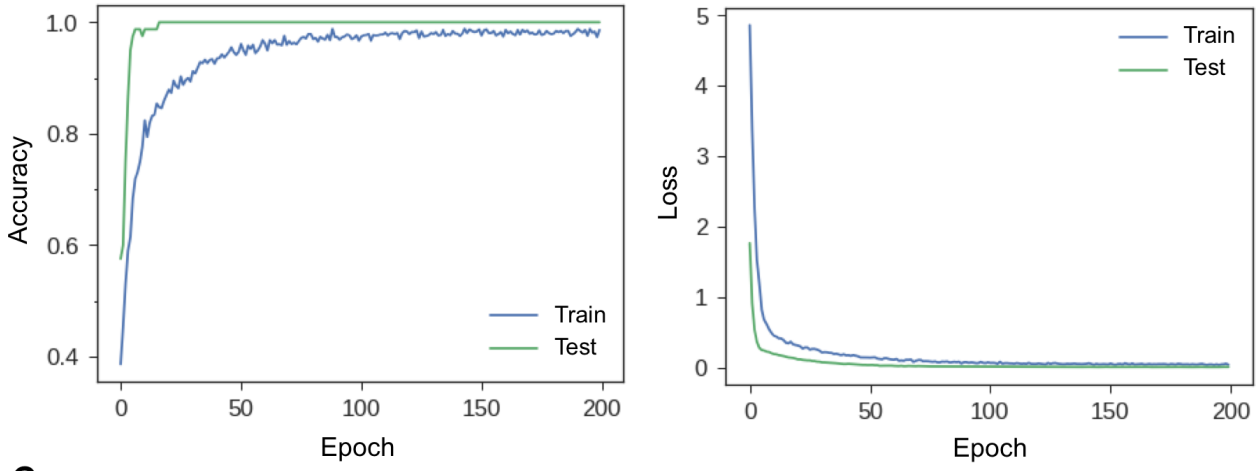

C

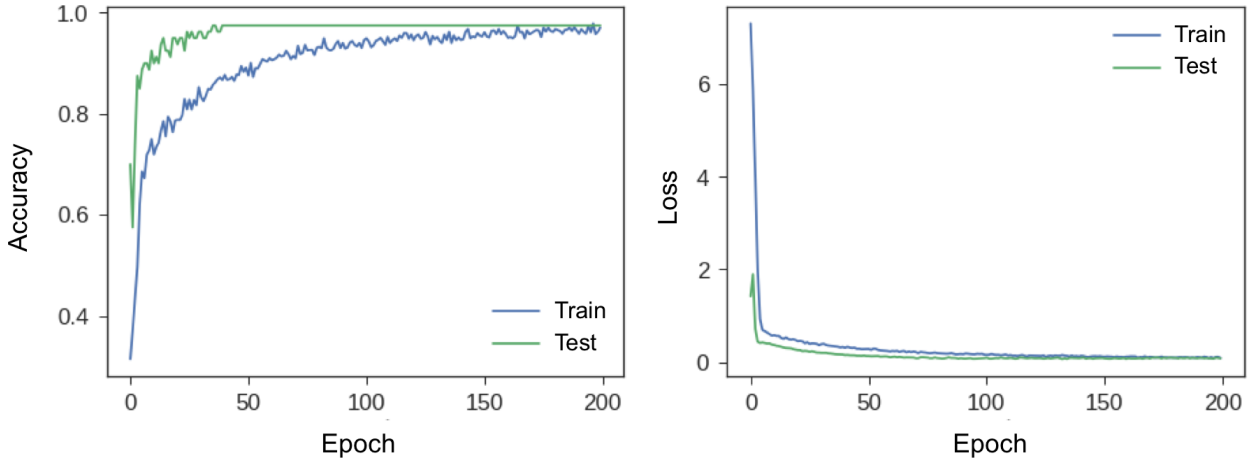

Figure 5. Classification results of the synthesized dataset. (A) Accuracy and loss results by the three machine learning approaches. **(B)** VGG-19-FC training trajectories with object images. **(C)** VGG-19-FC training trajectories with holograms.

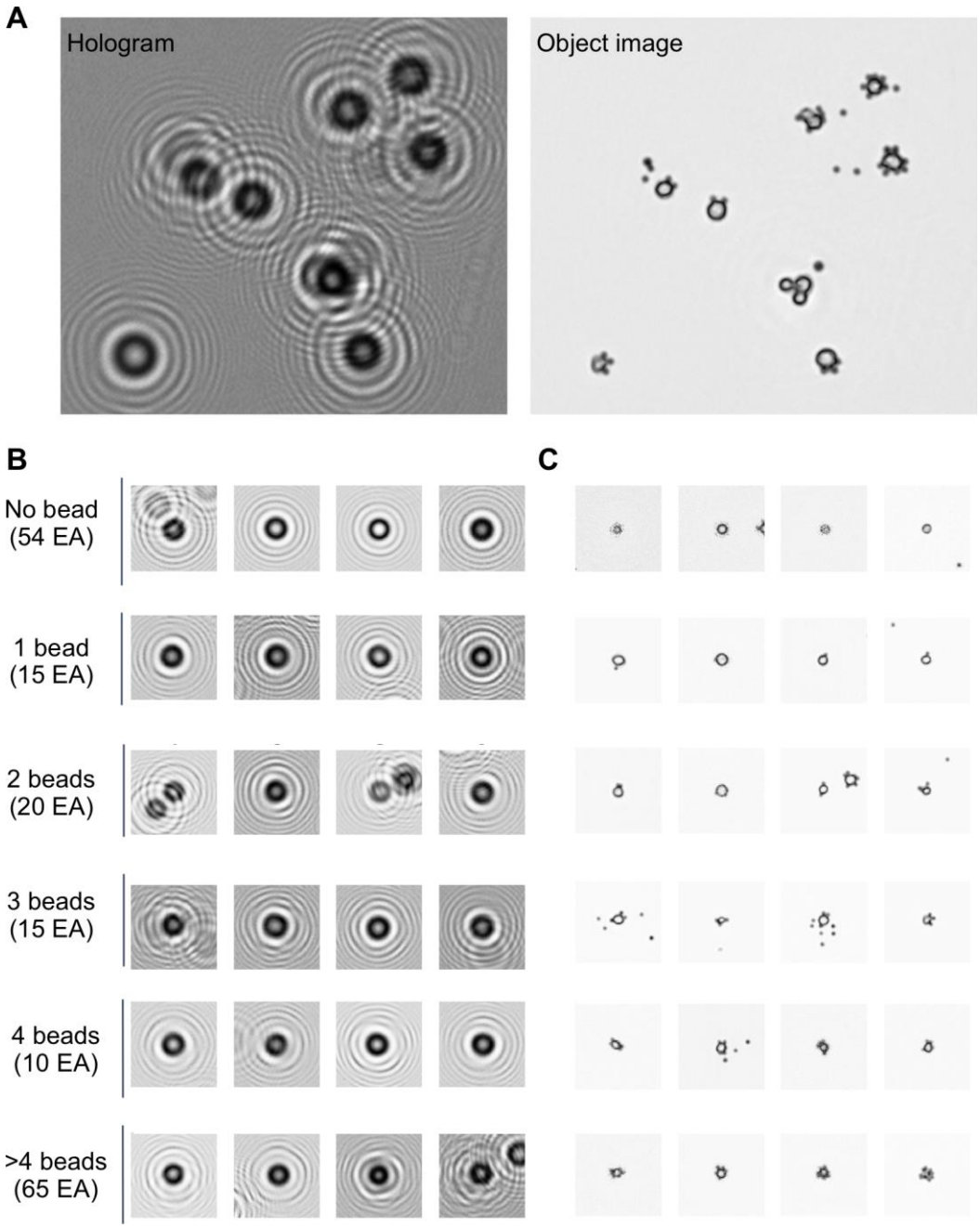

Figure 6. Experimental hologram dataset. (A) Experimental hologram and reconstructed image used for the preparation of training dataset. **(B, C)** Examples of hologram (B) and object images (C) in the training data. Each image has 270 × 270 pixels.

A

	Accuracy (%)		Loss	
	Object image	Hologram	Object image	Hologram
SVM	51.4	50.2	–	–
PCA-SVM	68.2	61.4	-	-
CNN	80.0	80.5	2.2	1.7
VGG-19-FC	94.4	94.4	0.3	0.2

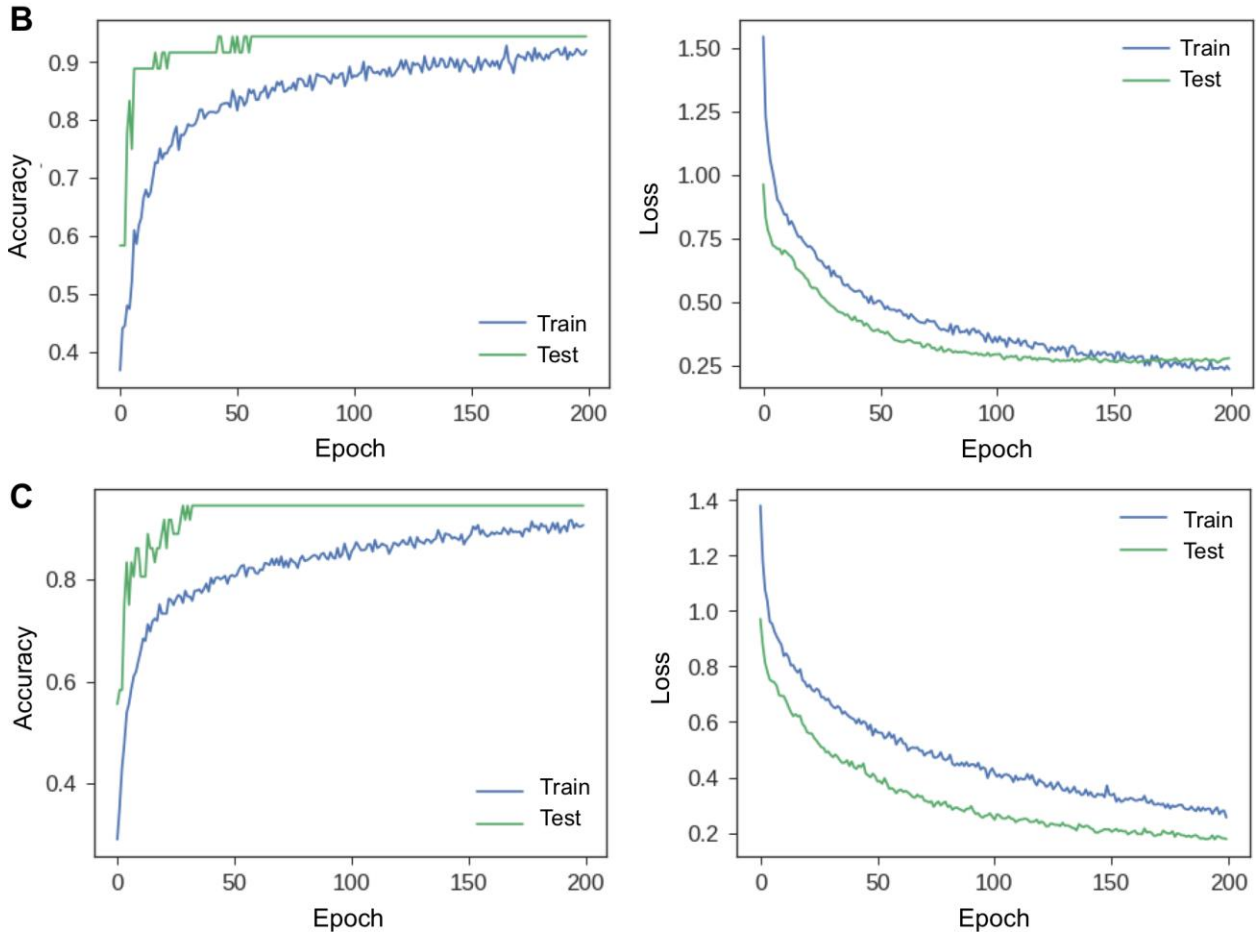

Figure 7. Classification results of the experimental dataset. (A) Accuracy and loss results by the three machine learning approaches. **(B)** VGG-19-FC training trajectories with object images. **(C)** VGG-19-FC training trajectories with holograms.

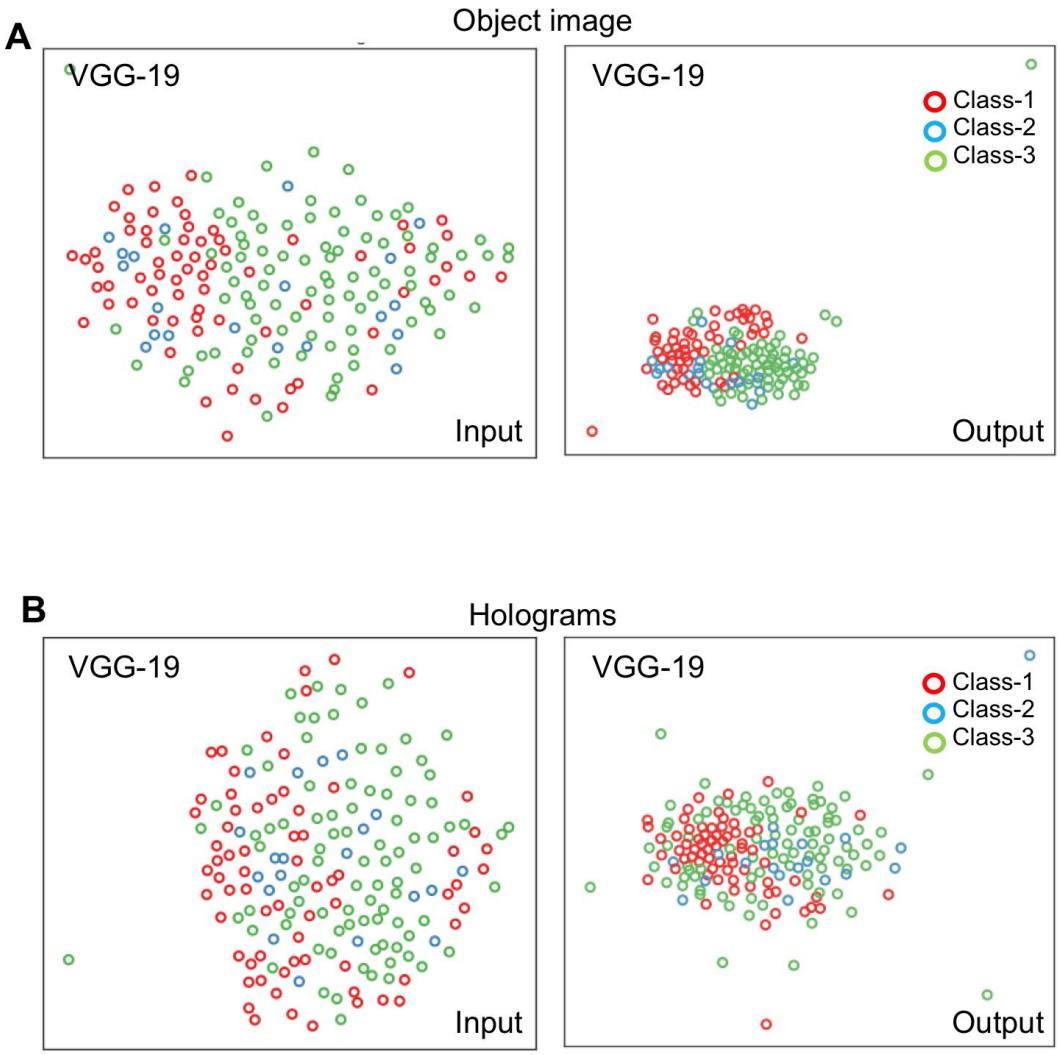

Figure 8. Classification results of the experimental dataset. (A, B) t-SNE results of inputs and outputs of VGG-19 pretrained in the case of object images (A) and holograms (B).